Gómez-Villalba, L.S., Sierra-Fernández, A., Rabanal, M.E., Fort, R. (2016). TEM-HRTEM study on the dehydration process of nanostructured Mg–Ca hydroxide into Mg–Ca oxide. *Ceramics International*, v. 42, pp. 9455–9466.
DOI: https://doi.org/10.1016/j.ceramint.2016.03.007

Published by Elsevier Ltd and Techna Group S.r.l.

TEM-HRTEM study on the dehydration process of nanostructured Mg–Ca hydroxide into Mg–Ca oxide

L.S. Gomez-Villalba [a,*], A. Sierra-Fernandez [a,b], M.E. Rabanal [b,c], R. Fort [a]

[a] Instituto de Geociencias (CSIC, UCM), Calle José Antonio Novais 12, 28040 Madrid, Spain
[b] Materials Science and Engineering Department Universidad Carlos III de Madrid, Avda. Universidad 30, Leganés, 28911 Madrid, Spain
[c] Instituto Tecnológico de Química y Materiales Alvaro Alonso Barba (IAAB), Avda. Universidad 30, Leganés, 28911 Madrid, Spain

Keywords:
Nanoparticles
Electron irradiation
Phase transformation
Brucite
Periclase
Mg–Ca hydroxide
Mg–Ca oxide

A B S T R A C T

The dehydration process from $Mg_{0.97}Ca_{0.03}$ $(OH)_2$ nanoparticles (brucite type hexagonal structure) to $Mg_{0.97}Ca_{0.03}O$ (periclase type cubic structure) was studied by Transmission Electron Microscopy (TEM-HRTEM), Electron Diffraction (SAED), Electron Energy Loss Spectroscopy (EELS) and image analysis. The transformation process was monitored in function of the reaction time applying 200 and 300 KV. Changes in porosity were possible to observe only during the irradiation with 200 KV. Depending on the irradiation time, the changes were gradual, producing an increase from the particle's edge towards the inner region. Different stages were observed, corresponding to the amount of water extracted from the particle, until finally a decrease in porosity and particle shrinkage occurs, coinciding with the formation of the Mg–Ca oxide. However, when samples were exposed to 300 KV, the dehydration process was much faster, and the pores structure was destroyed in a shorter time in comparison with lower doses of radiation. High resolution electron microscopy (HRTEM) applying 300 kV allowed identifying the progressive changes from brucite to periclase, including the formation of an intermediate dehydrated phase. The transformation along $[0001]_{brucite}$ and $[10\bar{1}0]_{brucite}$ orientations was monitored determining differences in the kinetic of reaction related to the presence of point defects affecting the atomic lattice.

1. Introduction

The irradiation of nanomaterials with electrons shows a great variety of fundamental importance phenomena that may be studied by in-situ electron microscopy. Modern TEMs offer the possibility to study materials with resolution down to 0.1 nm or even less, enabling the understanding of radiation effects at atomic scale. An advantage of *in-situ* electron microscopy is that structural transformations can be induced and imaged with the same electron beam and studied in real time with atomic resolution [1]. It has often been observed that a system relaxes from a metastable to the equilibrium state under the electron beam [1] .This is the case of porous solids, when used as catalyst or catalyst supports, that are frequently produced by dehydration of hydroxides. These materials show their importance in all applications due to their wide internal surface area on which adsorption and reaction can take place. The electron microscope technique not only enables the observation of these catalysts pore structure directly, but also the dehydration reactions to be followed *in situ* [2,3]. In inorganic materials, both knock-on and radiolysis may take place during their exposition to the electron beam, sometimes simultaneously. However, the radiolysis process has been observed predominantly in insulators (halides, oxides, hydrides, hydroxides, sulphides and silicates) while knock-on in conducting materials [4]. Radiation alters the physical properties of materials such as electro- conductivity, deformation, mechanical properties, etc. [5]. During the radiation, vacancies and interstitial atoms are grouped to form secondary defects such as clusters, dislocation loops and pores [5]. Although High-Resolution Transmission Electron Microscopy (HRTEM) is primarily a technique for studying bulk defects, it has been applied in the profile-imaging mode to derive information about surfaces [6]. Nowadays the EELS spectroscopy provides excellent alternatives to monitor the time evolution of chemical reactions [7,8].

Nowadays with the improvement in resolution, it is possible to observe the complex nanostructure of catalytic materials. There is no other experimental technique able to provide such a localized and direct view of both surface and bulk microstructure [9]. Spectroscopic measurements performed *in situ* within the microscope provide elemental analysis and give information on oxidation state

and bonding [10].The decomposition reactions represent an important class of solid state reactions, thus the understanding of their mechanism as well as kinetics is extremely important for synthesis of desired materials [11].

Most catalysts based on simple or mixed oxides are often derived from the dehydration of hydroxides. In the case of magnesium hydroxide, the dehydration technique is suitable for experimental investigation because of the existence of only two well-crystallized phases during the process, brucite ($Mg(OH)_2$) and periclase MgO [12,13], according to the following reaction:

$$Mg(OH)_2\ (\text{brucite})\ (s) \rightarrow MgO\ (\text{periclase})\ (s) + H_2O\ (g)$$

Brucite structure is representative of a group of bivalent metal hydroxides $M(OH)_2$ where M = Mg, Ca, Mn, Fe, Co, Ni or Cd with a compact hexagonal packing [14]. The structures are layered, where cations are placed in the octahedral interstices between two sheets of $(OH)^-$ arranged parallel to (0001) and every $(OH)^-$ is linked to three cations [15]. This structure is also common in other minerals, as brittle micas which are built up of alternate mica- and brucite-like layers [16]. The dehydration shows some common patterns of behaviour as the dehydroxylation processes of simple hydroxides ($Mg(OH)_2$, $Ca(OH)_2$ [17].

The reaction mechanism has been thoroughly studied in literature due to its wide application in decomposition of other hydroxides through a combination of different complementary experimental approaches [18,19]. In thermal dehydration, a simple $Mg(OH)_2$ crystal (P-3m1) with CdI_2 type structure is converted into a NaCl-type MgO cubic crystal (Fm-3m) [20], as a result of a topotactic reaction [21]. Previous studies of differential thermal analysis (DTA), thermogravimetry (TG) or in situ X Ray Diffraction [22–24] have permitted to delimit the transformation temperature between 300 and 350 °C, in $Mg(OH)_2$ nanoparticles obtained from different synthesis methods. On the other hand, $Mg(OH)_2$ could also be dehydrated by radiating with high-energy electrons [12,13,19,21,25]. During a TEM session, the local temperature reaches values between 500 and 600 °C [26]. Nowadays, the inclusion of a heating stage that is capable of rapidly heating the sample with minimal thermal drift has allowed to see high resolution images obtaining important advances *in* dynamic high resolution transmission electron microscopy during in *situ* Environmental-TEM experiments [27]. With this tool has been possible *to* understand the mechanisms of sintering in nanoscale particles [27] including the MgO by $Mg(OH)_2$ dehydration in a short time [28]. Thus, the transmission electron microscopy techniques result very useful for the understanding of the kinetics of brucite into periclase transformation.

Magnesium hydroxide has proven to be of great interest in medicine, industry, in environmental rehabilitation and recently in the conservation of cultural heritage [29], due to its outstanding physical and chemical properties. Brucite is an industrial mineral with an excellent market-growth potential. It also represents a potential ore source for the metal, magnesium, which is itself in high demand [30]. Such brucite and periclase can be used as catalysts [31], refractory [32], thermal insulator [33], fire retardant [34], or in steel coatings [35]. Also, brucite and periclase are used as reinforcement in nanoparticles for biomedical applications [36] and as anti-acid in the pharmaceutical industry [37]. Other applications include the use of $Mg(OH)_2$ for chemical heat storage in nuclear reactors [38,39]. Hence, tracking the process of dehydration by the electron beam is quite useful in the field of energy technology.

Catalysts containing two or more metals might show significantly different catalytic properties compared with the parent metals and thus might be widely used in several catalytic reactions [40,41]. There are many similarities between pure Mg hydroxide with Mg–Ca hydroxide, although the presence of calcium within the Mg structure could modify its behaviour. Dehydration process could have large implications when calcium is incorporated for obtaining Mg–Ca hydroxide, instead of having pure Mg hydroxide. This case is fairly frequent because many nanomaterials based on Mg hydroxides have been obtained by breaking down methods, for example the use of Mg–Ca precursors is very common in commercial products [19]. This is the case of Mg–Ca carbonate precursors obtained from calcination of natural geological deposits such as dolomite ($MgCa(CO_3)_2$), from dolostones, magnesite ($MgCO_3$), magnesia (MgO) or Mg–Ca oxide (more known as dolime, or burnt dolomite [42]).

On the other hand, many geological processes are associated with the presence of Mg–Ca hydroxides, such in metamorphic rocks. During metamorphism, the increasing of temperature on sedimentary or metasedimentary rocks including dolostones or dolomitic marbles, leads to the brucite dehydration to finally be transformed to periclase [43]. Besides, it is also common in magnesium–calcium ultramafic rocks such as dunite and peridotite [16] usually used in the construction industry [30].

These work results will provide remarkable information in different aspects, where is convenient the use of Mg and Ca hydroxides as co-catalyst, consolidating or fire retardant. As consolidant is frequently used in stones [44] artistic works, including cellulose-based products (canvas, paper or wood) [45, 46], where the use of nanostructured Mg and Ca hydroxides are the most suitable consolidant to control decay-induced deacidification process [47]. Also, in the field of ceramics, glass ceramics and construction materials industry, including mortars, concrete or cement to modify its properties [30]. The present study aims to contribute to the understanding of the transformation kinetics of Mg–Ca hydroxide to Mg Ca oxide by means of TEM-HRTEM, electron diffraction, electron energy loss, and energy-dispersive x-ray spectroscopy techniques. The *in-situ* evolution of the Mg–Ca hydroxide has been carried out using different transmission electron microscopy techniques. The main objective is to evaluate and point out the changes in morphology, porosity, structural defects, phase transformations or chemistry as a result of the exposition to the electron beam applying acceleration voltages of 200 and 300 kV.

2. Experimental

The commercial product Mg–Ca hydroxide (SSA: ~80 m^2/g) supplied by Nanostructured & Amorphous Materials Inc has been used in the process of dehydration. The TEM samples were taken from ultrasonically dispersed acetone suspensions. A drop of each suspension has been placed on a copper grid with a holey carbon film cover and examined under TEM.

The JEOL-JEM 2100TEM microscope, operating at 200 kV (0.25 nm point to point resolution) equipped with selected area electron diffraction (SAED) and energy dispersive X ray detector (EDS -OXFORD INCA) was used for studying the porosity evolution with the irradiation time and for analysing the chemical composition. A representative particle was selected to follow the porosity along the electron beam irradiation. In all cases, very thin edges of the particle were chosen to avoid multi-dispersion effects and ensuring reliable images. The interpretation has been carried out taking into account the phase contrast effects, which were carefully monitored according to the methodology of Edington [3]. The images were acquired since the beginning of irradiation until the final stage when the particles collapsed. The image J software has been used to calculate the porosity obtained from isolated and very thin particles at low magnification TEM images.

The high resolution TEM study has been carried out in a

JEOL-JEM 3000 operating at 300 kV (measurement conditions: lens aperture, 60 μm; condenser aperture, 70 μm; focal beam spot diameter, ~3 nm, 0.17 point to point resolution). The interpretation includes the use of Fourier filtered technique for obtaining Fast Fourier transformed (FFT). The chemical analyses have been carried out using energy dispersive X ray spectroscopy (EDS) and Electron Energy Loss Spectroscopy (EELS). A Gatan Enfina filter equipped in the Jeol Jem 3000 TEM was utilized to detect electron energy loss spectra. The analysed surface with the EEL detector was ~2–3 nm, with an energy dispersion of 1.0 eV/channel, a collection angle of 8 mrad and a convergence angle of 9 mrad. A total of 100 EELS spectra taken parallel to *c* axis were recorded in diffraction mode. The EELS database was used for comparing the obtained results with the reference spectra [48]. Gatan Digital Micrograph software was used to process High Resolution Transmission Electron Microscopy images (HRTEM), EELS and Selected Area Electron Diffraction (SAED) patterns. Calculated electron diffraction models were developed with Electron Diffraction Pattern Simulation software v 7.2 (Diffract) [49].

The EEL spectra have been modelled by a power law background [50]. Fourier-log deconvolution has been used to remove the plural scattering. The particle´s thickness has been calculated extracting the zero- loss peak and using the Kramers-Kronig sum rule [50]. A relative thickness over the irradiated area (t/λ)) was calculated, being λ (in nm) the mean free path of inelastic electron scattering (MFP). Measurements have been carried out, at the beginning and at the end of the irradiation period, to calculate possible differences in the thickness.

3. Results and discussion

3.1. General aspects (low magnification TEM-electron diffraction)

The Mg–Ca hydroxide nanoparticles tend to suffer reduction when are exposed to the high-energy electron beam. During irradiation, fresh brucite (Fig. 1a and c) is gradually transformed into periclase (Fig. 1d) to finally lose its crystallinity (Fig. 1e).

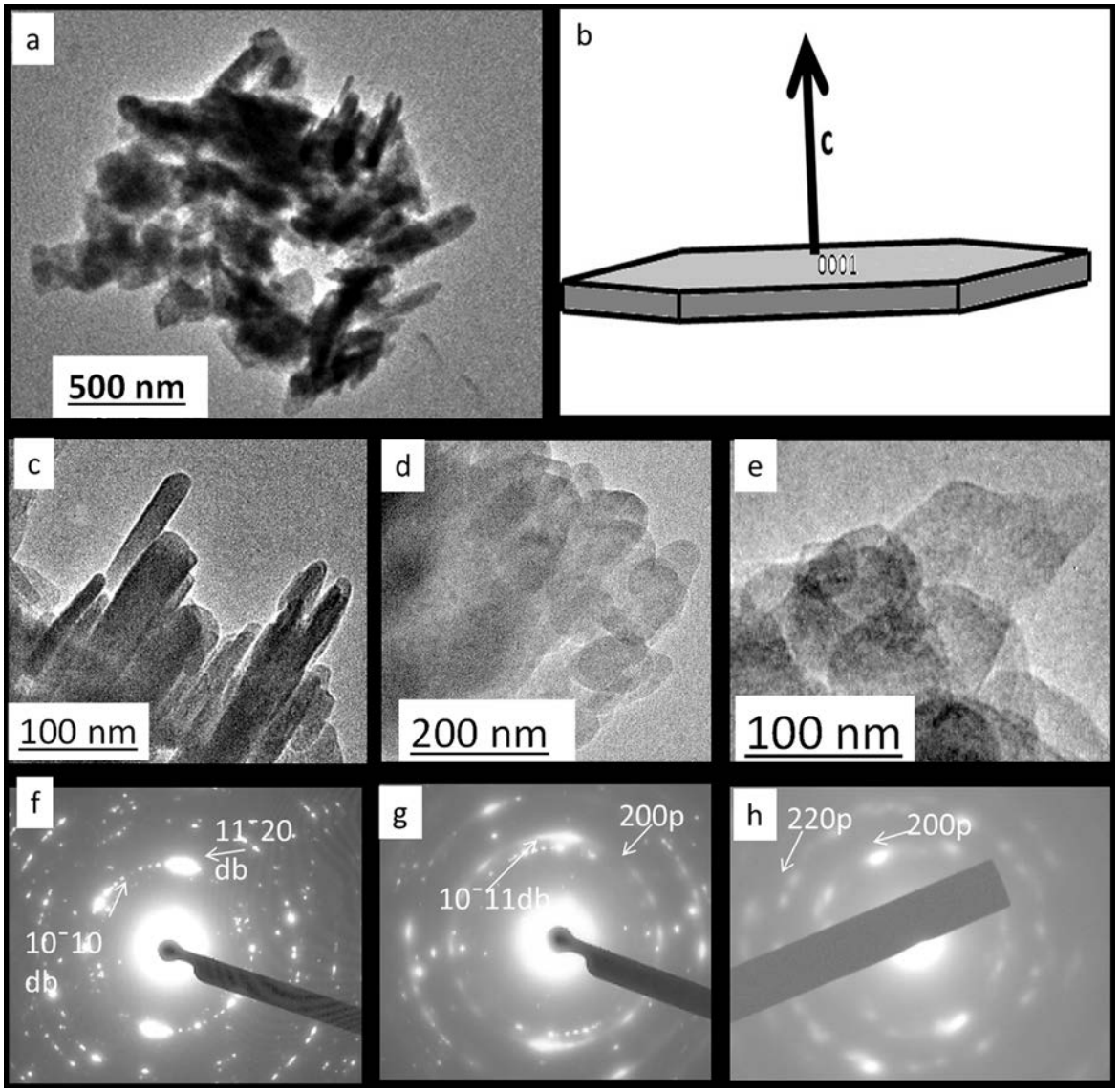

Fig. 1. Low magnification TEM images in bright field mode and SAED patterns. General aspect of the $Mg_{0.97}Ca_{0.03}(OH)_2$ nanoparticles before the irradiation (a) and the progressive changes in nanoparticles during the exposition to electron beam (c, d and e). Details of the process showing changes in lamellar crystals of brucite, in the early stage of radiation (c), intermediate (d) and final stage when the amorphisation is produced (e). The *I*dealised model of a brucite crystal is shown in b. The corresponding polycrystalline SAED patterns from dehydrated brucite (f), in an intermediate stage with simultaneous presence of dehydrated brucite (db) and periclase (p) (g) and textured ring pattern after ~700 s of irradiation indicating high structural disorder of periclase. (h). TEM operating at 200 kV.

In general, subparallel aggregate of lamellas ranging from 250 to 390 nm (longer length) and 30 to 120 nm (shorter length); or fibrous shapes are observed at the beginning of the exposition (Fig. 1a and c). The idealized model is shown in Fig. 1b. When the particles are exposed to 200 kV, the dehydration process occurs at intervals of ~10 to ~700 s depending on the particle thickness. Particles undergo a change in both its morphology and its crystallinity. Thus, particles with tabular shapes, fibrous aggregates with corroded edges or massive appearance are formed (Fig. 1d), suggesting poor crystallinity or amorphisation conducing to a fully dehydrated brucite (Fig. 1e). This loss of crystallinity occurs under the electron beam at both high and low flounce rates [51], due to radiation in high doses of which could generate amorphous zones with critical concentration of vacancies in the material [5].

The chemical concentration obtained by EDS indicates a proportion of Mg: 32.07 atomic %, Ca: 0.87 atomic %, O: 67.06 atomic %, obtaining the solid solution with formula $Mg_{0.97}Ca_{0.03}(OH)_2$. This previous solid solution is stable considering the ionic radii of Mg^{2+} (0.72 Å) and Ca^{2+} (1.00 Å) [52].

3.2. Porosity changes during the exposition at 200 kV

The dehydration process of Mg–Ca hydroxide to produce the corresponding Mg–Ca oxide modifies the porosity because of water release. Changes in the particle´s porosity were monitored during their exposure to the electron beam at 200 kV, after 10, 152,224 and 700 s. The Fig. 2 shows the different steps during the exposition, and the calculated porosity obtained for each time in a particle with particle´s size around 300 nm. The bright regions in the experimental images are interpreted as pores while the dark areas in the calculated images correspond to porous surfaces.

At the beginning, the formation of an elongated and rounded pore system is focused on the particle edge and along the cleavage surfaces, with a variable pore sizes between 2 and 13 nm (Fig. 2a). During the irradiation time, these pores tend to enlarge in size, so that after 152 s, the pores are few, small and rounded (5–8 nm, and 15–25 nm) (Fig. 2b), after 224 s (Fig. 2c) a pore size up to 45 nm can be reached, although smaller pores (15–30 nm) are predominant. Similarly, pores begin to be created in the innermost of particle areas. The augment of pore size gives rise to an increase in porosity (Table 1). So, finally the particle edges are the surfaces where highest porosity occurs, with 11% at the beginning of the exposition (Fig. 2a and a'), reaching 44.8% after 224 s of irradiation (Fig. 2c and c').This increase is produced by the coalescence of pores (Fig. 2e–e').

An augment of porosity inside the particle (from 13.6% to 21.8%) is observed when the radiation time reaches 224 s (Fig. 2b–b' and c–c'). After 700 s, there is an enormous change in the pores´s behaviour (Fig. 2d, d', and f, f'). At the shorter exposure time, the porosity increases in both external and internal zones, however, after prolonged radiation times, the porosity decreases dramatically, reaching only 7% at the edges and 3.7% inside the particles. Besides, pores do not surpass 6 nm in its largest diameter (Fig. 4f–f'). (Table 1)

The dynamic of porosity formation observed during irradiation starts at the particle edge, gradually increasing towards the interior. However the dehydration process happens simultaneously everywhere, especially at the electron-exit surface. Consecutively, the pore size is increased to finally collapse the structure with a decrease in porosity and pore size, as described in pure brucite particles [53].

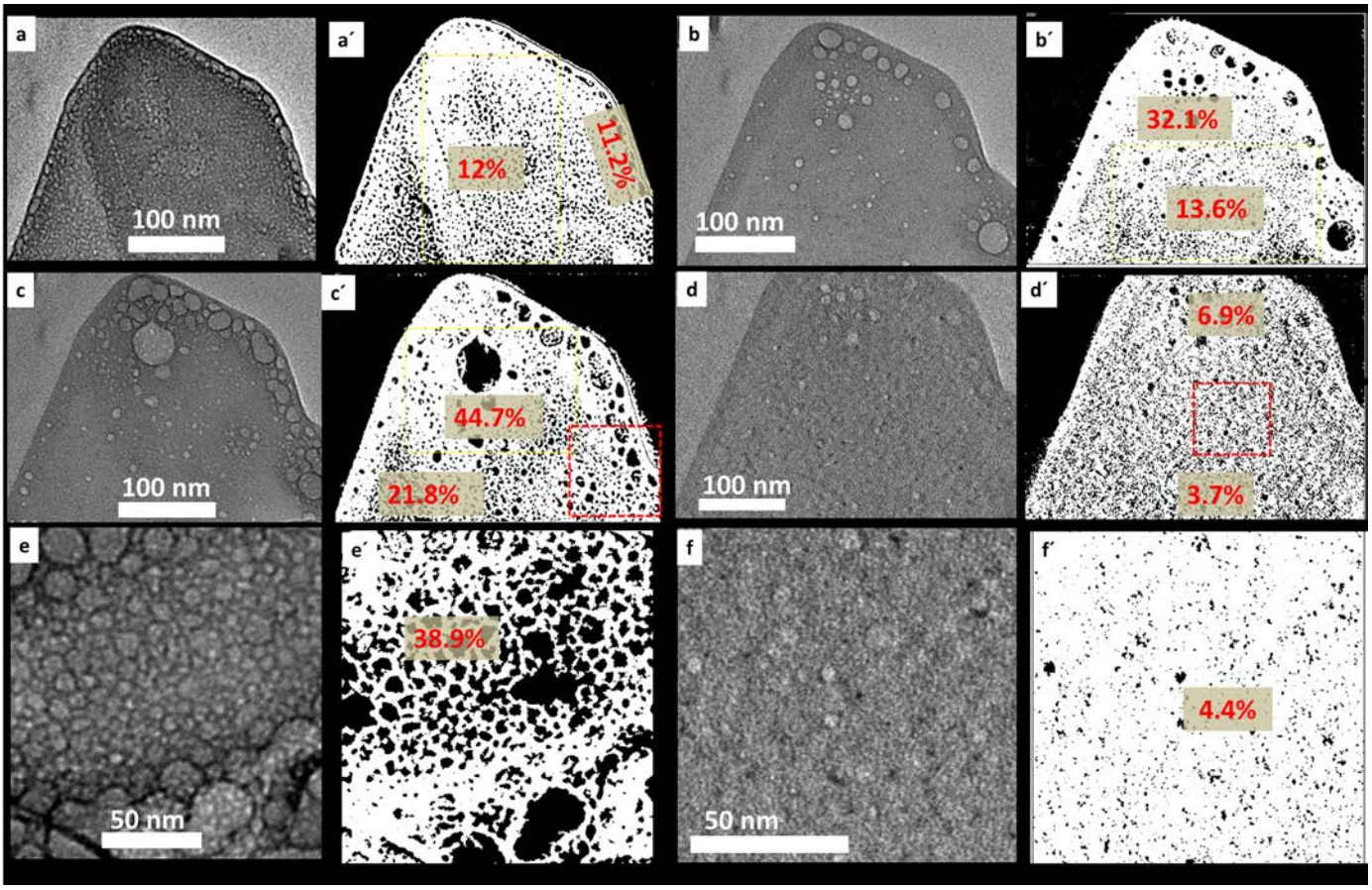

Fig. 2. Low magnification TEM images obtained during the exposition at 200 kV, and the calculated porosity images obtained for each time of radiation: 10 s (a), 152 s (b), 224 s (c) and 700 s (d) with their corresponding calculated porosity (a', b', c', d'). A magnification of the porosity is presented at 224 s (e) and 700 s (f) with the respective calculated areas (e') and (f'). The dark areas of the particle delimited in the calculated images correspond to porous surfaces. TEM operating at 200 kV.

Table 1
Calculated porosity values obtained from an isolated particle during the exposition at 200 kV.

Time of exposition at 200 kV (s)	Outer region		Inner region		Remarks
	Porosity (%)	Pore size (nm)	Porosity (%)	Pore size (nm)	
10	11	12 ± 1	12	2.5 ± 0.5	Predominant elongated pores at the edge and along the cleavage surfaces. Rounded pores in the inner region
152	32.8	20 ± 5	13.6	6.5 ± 1.5	Increase in pore size in both regions, particularly bigger pores in the outer region
224	38	30 ± 15	44.7	5.5 ± 1.5	Hugh pores in the outer region, due to coalescence of pores in internal and external regions. Internal region with differences in porosity
700	7	15 ± 5	3.7	< 6	Reduction in porosity and pore size.

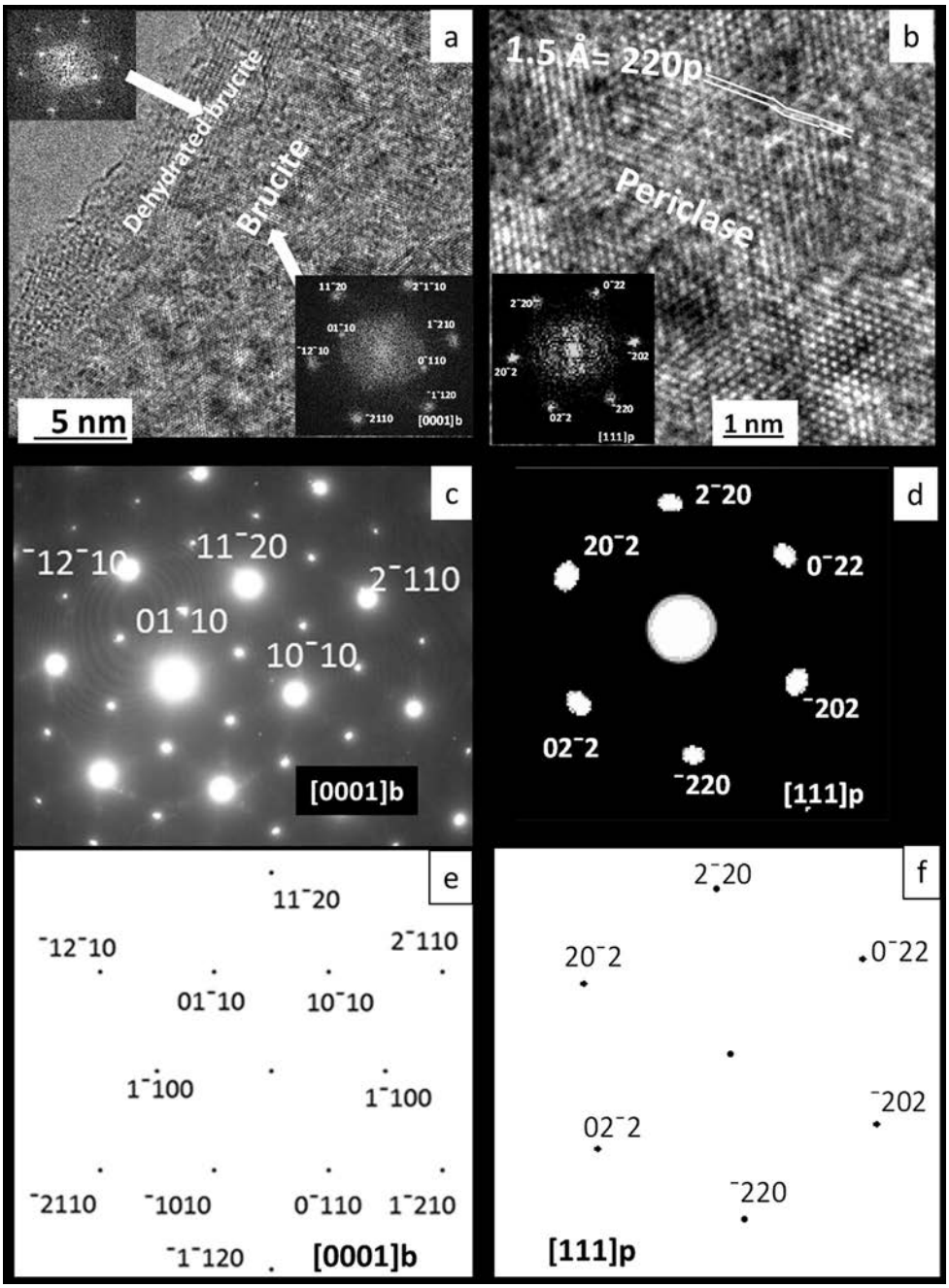

Fig. 3. HRTEM images showing the structural transformation from brucite to periclase in an early step of irradiation (a) and after 25 s of radiation (b). The dehydrated phase is beginning to form at early stage of irradiation (a) meanwhile the periclase is quickly formed (b). Some stacking faults affecting the neo- formed periclase phase are easily visible. The corresponding FFT confirm the structures (inset). The topotactic transformation is observed along the [0001] brucite to be converted into [111] periclase, as observed in the corresponding SAED patterns taken before (c) and after (d) irradiation process. The corresponding calculated electron diffraction patterns are shown in e and f respectively. TEM operating at 300 kV.

The changes in porosity are difficult to be controlled when the sample has been radiated at 300 kV. In this case the dehydration process is much faster, and its pores structure is destroyed in a shorter time in comparison with lower doses of radiation. This dehydration process has been tracked in other hydroxides, such as $Co(OH)_2$ to form CoO which has the same brucite structure (as $Ni(OH)_2$) with some common patterns [2,18]. The dehydration process usually begins at the edge of the specimen and progresses towards the centre. Also, the reaction at the interface involves the advance of pores. A similar situation has been observed during dehydration of $Al(OH)_3$, with the formation of narrow slit-like pores parallel to the original layer[3].

In this study, when applying a 200 kV acceleration voltage, the dehydration process takes place between 10 s and 700 s. Nevertheless, it could vary depending on grain thickness or voltage applied, as has been observed in the transformation of iron hydroxides (goethite-hematite), which occurred between 10 s and 20 min using a 100 kV beam [54].The present results are considered to be functional for different materials. The tracking of the dehydration process is very important because the retention of water within the porous structure is a key factor in determining reaction rates; in addition to the scale of the porous microstructure produced [54], as in the case of catalytic [55] or magnetic [56] materials among others. Nevertheless, these calculations are indicative, and detailed comparison between observed pore sizes and densities with those calculated from other techniques (gas absorption analysis, for instance) is necessary, before detailed conclusions may be drawn about the surface area available for catalysis [3].

3.3. Structural changes during the exposition at 300 kV

The structural evolution during the exposure to electron beam radiation is clearly seen from the results of selected area electron diffraction (SAED) in combination with high resolution TEM images (HRTEM) and Fourier transform calculations (FFT). This monitoring is performed by the electron beam at 300 kV, because it is possible to get more suitable and valuable information due to its higher resolution power.

3.3.1. Electron diffraction (ED)

The SAED patterns taken both at the beginning and at the end of the irradiation allow to identify the brucite structure just in the early stage of *in situ* Mg Ca hydroxide/ MgCa oxide transformation as observed along [0001] zone axis (Fig. 3c). Besides, just at the end of the exposure to the electron beam, the SAED pattern shows the typical periclase structure along the [111] orientation (Fig. 3d). This change is observed both at 200 and 300 kV confirming the topotactic relationship $[11\bar{2}0]_{brucite}$ (1.5 Å)//$110_{periclase}$ (1.48 Å) [12,13]. This relationship may be observed also from the calculated electron diffraction patterns (Fig. 3e and f).

The calculated cell parameters obtained from SAED and FFT for $Mg_{0.97}Ca_{0.03}(OH)_2$ and $Mg_{0.97}Ca_{0.03}O$ are different to the typical brucite and periclase phases. Thus, these values were $a=b=3.1292$ Å, $c=4.8222$ Å for the hydrated phase ($Mg(OH)_2$reference pattern: jcpdf 44-1482, $a=b=3.144$ Å, $c=4.777$ Å) and $a=b=c=4.1128$ Å for the dehydrated phase (MgO reference pattern: jcpdf 78- 0430, $a=b=c=4.212$ Å).

An overview of this behaviour is derived from the ring patterns taken along the decomposition process (Fig. 1f, g and h). Since the specimen is highly reactive, the initial brucite (Fig. 1f) is quickly dehydrated forming an intermediate phase (labelled as dehydrated brucite "db"), which is obtained in short times of exposition (~10–20 s) (Fig. 1f and g). The intermediate phase presents a reduction in the interplanar spacing (2.6 Å, 2.28 Å, 1,52 Å and 1.42 Å) in comparison to the typical brucite structure (jcpds=44-1482, strongest intensities of d $_{hkl:}$ 2.7 Å (100), 2.36 Å (101), 1.57 Å (110) and 1.49 Å(111) respectively).

The shrinkage of the atomic distances is inherent to the decomposition process and it has been previously reported [12,13,19,21].Similarly, the transformation indicates the simultaneous presence of dehydrated brucite and periclase(Fig. 1g), which subsequently results in a highly textured pattern of periclase, where a high content of structural defects occurs (Fig. 1h).

According to Goodman studies [21], the basal plane shrinks in the first stage, generating stress that cracks the crystal. This change is followed by a collapse in magnesium hydroxide planes under the [0001] orientation. The collapse is also governed by inter-plane water molecule migration to an exit surface [21]. According to author´s finding, the magnesium oxide formed is highly oriented. Goodman found that the decline in the brucite basal plane distance (from 3.12 Å to 2.99 Å) is induced by a change in the Mg–Mg distance, which agreed with the magnesium oxide plane (111) distance [21].

3.3.2. High resolution TEM (HRTEM)

Changes in a particle before (Fig. 3a) and after 25 s of electron beam irradiation (Fig. 3b) are clearly visible from HRTEM images, showing differences between the edge and the internal zone. At the beginning, the lattice image shows the internal region where the atomic planes have the typical arrangement of the brucite structure along the [0001] zone axis; nevertheless, in the particle edge the interatomic distances are slightly different but conserving the same brucite type structure, as confirm the respective optical diffraction for both, inside and outside regions (Fig. 3a inset).These changes in the atomic distances suggest an intermediate phase, product of dehydration process, where some vestiges of porosity are also observed.

After 25 s of exposure (Fig. 3b), the $Mg_{0.97}Ca_{0.03}(OH)_2$ with brucite-type structure, oriented along the [0001] zone axis has been converted to $Mg_{0.97}Ca_{0.03}$ O oxide with periclase-type structure, acquiring the [111] orientation as shown in HRTEM image. Some stacking faults (SF) affect the (220) planes of the recently formed periclase phase. The corresponding FFT (Fig. 3a and b, inset) clearly points out the difference before and after irradiation. In this case, the $[10\bar{1}0]_{brucite}$ disappears and the $[11\bar{2}0]_{brucite}$ (Fig. 3c, inset) is transformed to $\{220\}_{periclase}$ as confirm the SAED patterns (Fig. 3d, inset). The calculated SAED patterns are presented in Fig. 3e and f respectively. In this case, the amorphisation process along the $[0001]_{brucite}//[111]_{periclase}$ is completed after 204 s of irradiation.

Similarly, the shrinkage of the structure during the brucite (Fig. 4a, c, e and g) to periclase transformation (Fig. 4b, d, f and h) is perceptible from HRTEM images and FFT. Fig. 4a shows a particle in an early step of irradiation, where the distances between lattice fringes adjust to the brucite structure oriented according to the $[10\bar{1}0]$ zone axis. In the inner region the $d_{(01\bar{1}0)}$ (2.7 Å) atomic planes are clearly visible, as confirms the optical diffraction (Fig. 4a and g). The angle between $d_{(01\bar{1}0)}$ (2.7 Å)and $d_{(01\bar{1}2)}$ (1.8 Å) is 48°, similar to the typical hexagonal arrangement along the $[10\bar{1}0]_{brucite}$ zone axis. Besides, certain disorder degree is evidenced by the presence of extra atoms, stacking faults and dislocations (Fig. 4c and e). These point defects are labelled in the micrographs with Burgers vectors, arrows and circles. An enlargement of the left edge (Fig. 4c) shows the basal plane $[10\bar{1}0]_{brucite}$ (2.7 Å) affected by stacking faults (SF), formed by local strain fields generated due to water leakage.

In Fig. 4b, the image was taken after 80 s of radiation. In this case, the $d_{(01\bar{1}0)}$ has been reduced from 2.7 Å to 2.04 Å. After irradiation, some extra atoms are still present (Fig. 4e), with less disorder degree in the atomic lattice (Fig. 4e). The optical

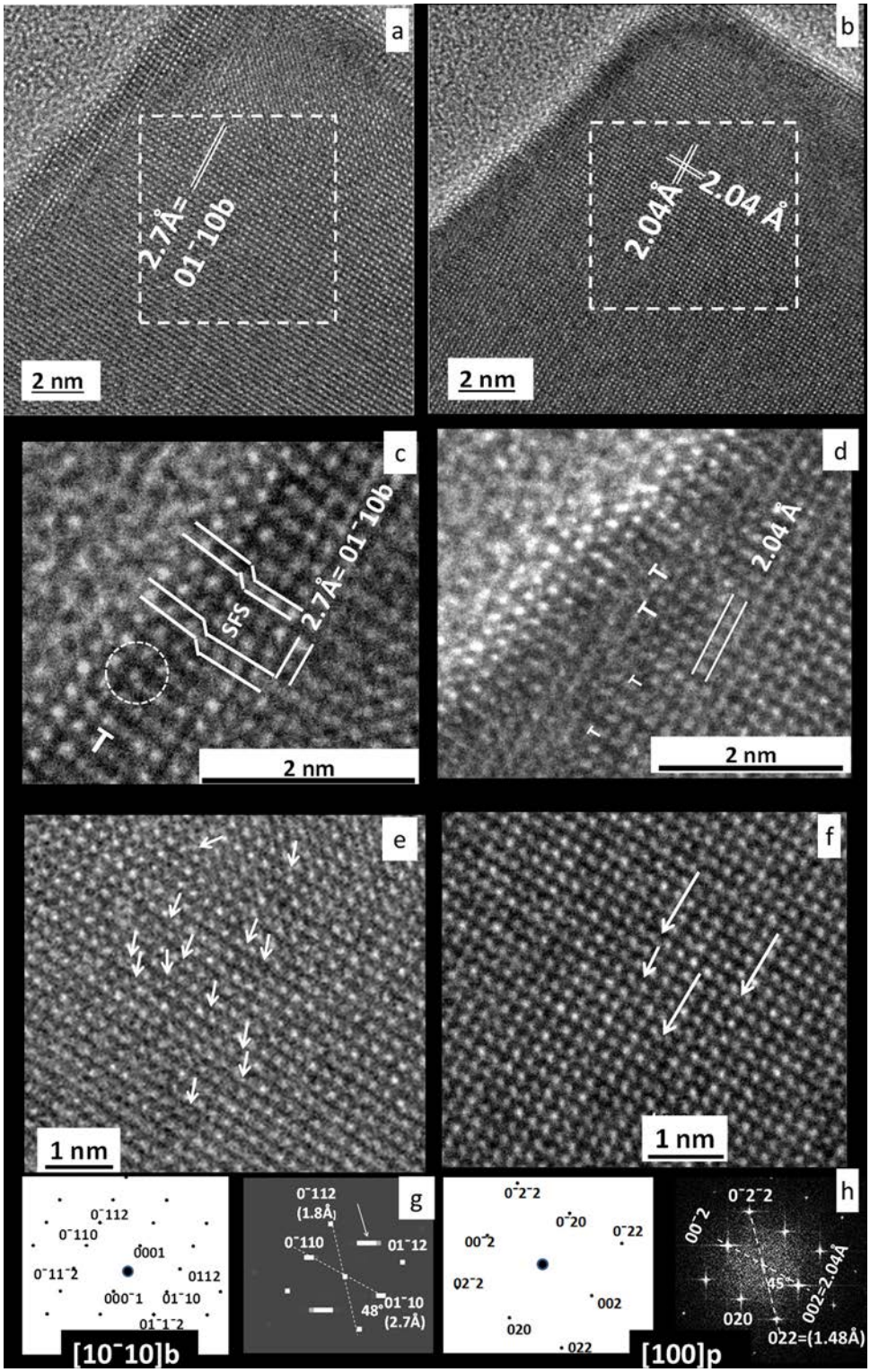

Fig. 4. HRTEM images showing the transformation of $[10\bar{1}0]_{brucite}$ into $[100]_{periclase}$. An enlargement image shows some stacking faults (SFS) affecting the $[10\bar{1}0]$ brucite plane at the beginning of the irradiation (c). After 80 s of irradiation, the atomic planes are transformed to {002} periclase, with some defects affecting the basal plane (d). Lattice image showing extra atoms present mainly in the dehydrated brucite (e) and in the new formed periclase phase (f). The corresponding calculated SAED (left) and FFT (right) patterns are presented before, (indexed as brucite) along $[10\bar{1}0]$ (g) and after (indexed as periclase) along [100] zone axis (h). Point defects are labeled with Burgers vectors, arrows and circles. TEM operating at 300 kV.

diffraction taken from the area shown in inset is indexed on the basis of a unit cell with periclase structure (Fig. 4f). The angle between $d_{(002)}$ (2.04 Å) and $d_{(022)}$ (1.48 Å) is 45°, corresponding to the cubic arrangement along the $[100]_{periclase}$ zone axis. Besides, the presence of dislocations affecting the {020} atomic planes is common in the rim (Fig. 4d).

The calculated SAED and FFT patterns taken before and after electron beam exposure (Fig. 4g and h, respectively) are consistent with diffraction patterns expected from brucite and periclase. The streaking observed in the early stage of dehydration (Fig. 4g-right)

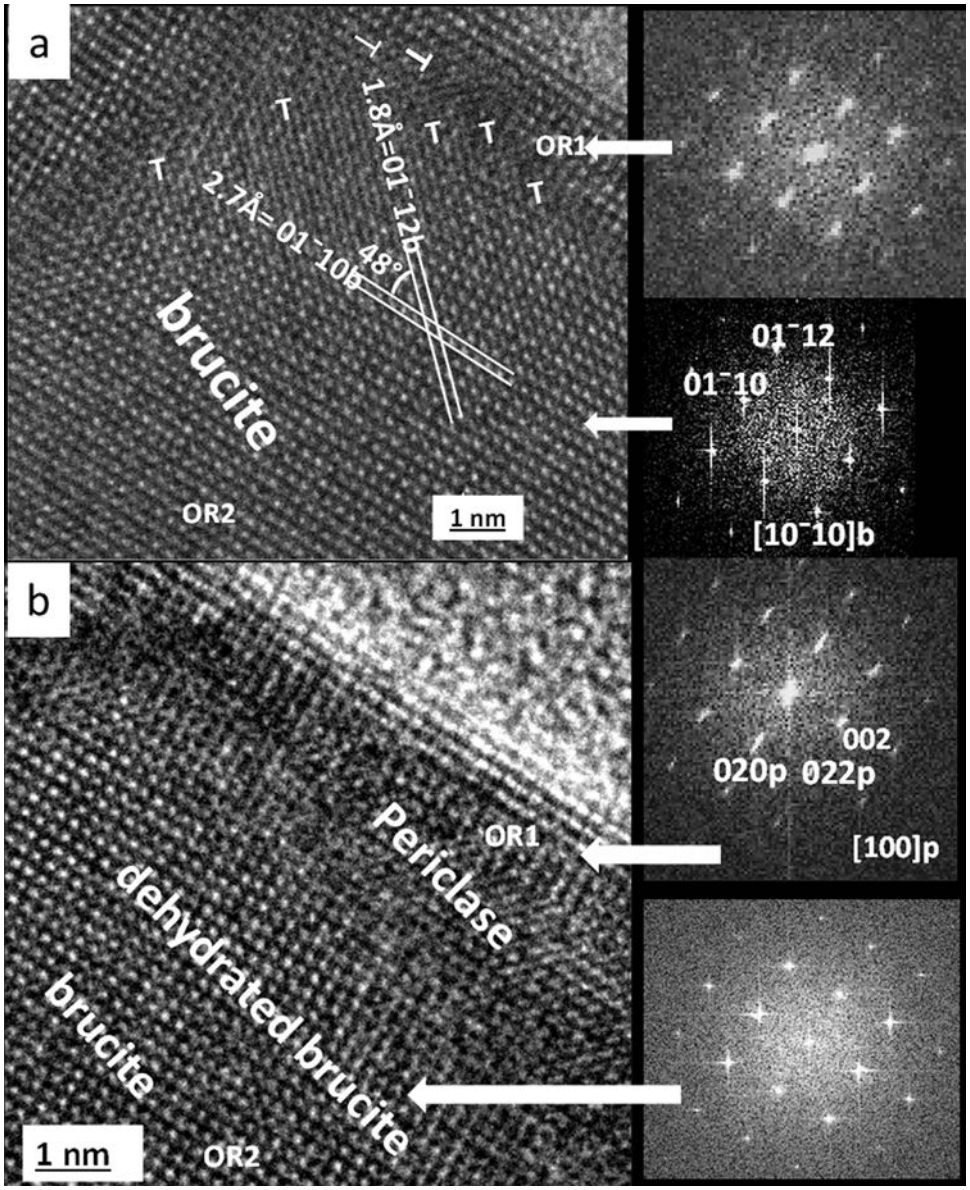

Fig. 5. An amplification of Fig. 4 showing details of the transformation from the initial brucite (a) with two orientation relationship (OR). After irradiation, the external region (OR1) is transformed to periclase, while the internal region corresponds to dehydrated brucite (OR2). The core is still brucite. The FFT before irradiation is indexed as brucite (a right) and after irradiation as periclase (b right). Textured FFT patterns of OR1 are due to shape effects. TEM operating at 300 kV.

is due to the presence of extra atoms (indicated by an arrow) present mainly in the dehydrated brucite.

The transformation process is not homogeneous as deduced from calculations based on FFT measurements. Some details of this transformation are magnified in Fig. 5.

Brucite is initially transformed into periclase; though, there are several regions in the particle where the dehydration process has been slower. While the inner retains the typical brucite structure (Fig. 5a), toward the particle edges, an intermediate phase of dehydrated brucite whose distances are different enough from the typical brucite structure is developed, confirming the information from the electron diffraction patterns (Fig. 1g). Nevertheless, the edge coincides with the periclase type structure (Fig. 5b).

The indexed Fourier Transforms taken from the regions indicated by arrows (OR1 and OR2) are shown as insets (Fig. 5a). The indexing corresponds to brucite in the early stage of irradiation. In the FFT (top right-OR1), the streaking observed at the rim runs perpendicular to habit plane, (affecting the basal plane) is due to shape effects [3]. But when the FFT is taken in the inner region (OR2) the typical brucite structure along [1010] is still present.

After the irradiation, (Fig. 5b, right top inset) the optical diffraction shows the same streaking, but the indexing corresponds to periclase along [100], just in the border of the particle. Nevertheless, In the inner, the spots on the FFT (inset in Fig. 5b, right bottom) correspond to an intermediate phase of the dehydrated brucite.

The interplanar spacing calculated from the FFT indicates variations during the different times of exposure to the electron beam, as a function of water loss. A similar situation occurs in the decomposition of iron hydroxide (goethite- hematite transformation) [54].

The regions (OR1) and (OR2) observed in HRTEM images corresponding to the newly formed dehydrated periclase and brucite respectively, are similar to the acceptor and donor regions identified by Ball [12]. The donor region (brucite) is completely deteriorated with high porosity area, and the acceptor with parts that are converted into periclase [21]. The presence of an intermediate phase has been also reported in pure brucite during TEM

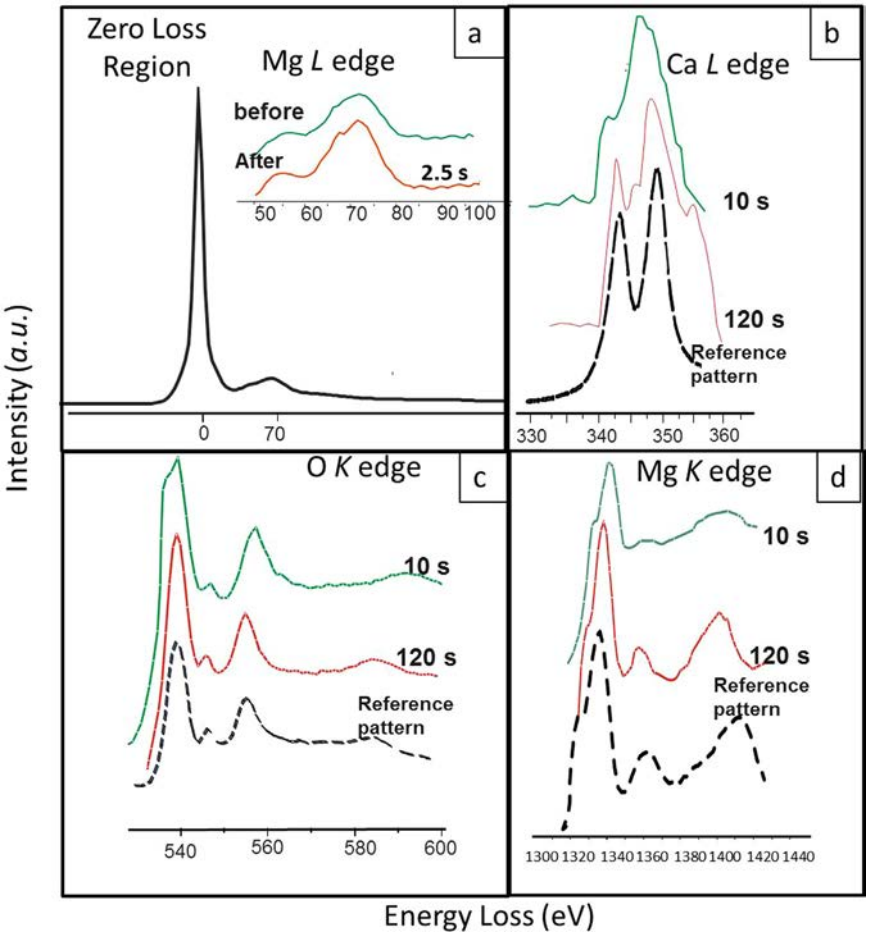

Fig. 6. *in situ EEL* spectra taken during dehydration of $Mg_{0.97}Ca_{0.03}(OH)_2$ by electron beam irradiation. a: the zero loss and low loss for Mg *L* edge (as inset). b: Ca *L* edge, c: O *K* edge d: Mg *K* edge. The spectra are compared to the reference pattern from EELS database [48]. Spectra were taken parallel to c axis. The spectra are displaced vertically for ease of comparison. TEM operating at 300 kV.

irradiation [21]. The host lamella (brucite) would guide the formation of a solid solution series of lamellar oxy-hydroxide intermediates in route to oxide formation [25].

3.4. Chemical behaviour during the irradiation

The chemical behaviour during the exposition to electron beam energy at 300 KV, resulting in the dehydration of $Mg_{0.97}Ca_{0.03}(OH)_2$, is followed by the electron energy loss spectroscopy (EELS). Spectra have been acquired parallel to $[0001]_{brucite}$, corresponding to the first time of the dehydration, and just before the total decomposition. Results presented have been followed in low and high electron energy loss regions, corresponding to Mg *L*-edge, Ca *L*-edge, O *K*-edge and Mg *K*-edge. The spectra are displaced vertically for ease of comparison.

3.4.1. Low loss region and Mg L-edge

The zero- loss peak and the low loss region (as inset) are shown in Fig. 6a. The low loss region shows two plasmon peaks in the range to about 50 eV to 100 eV. Both peaks correspond to the Mg *L* edge, at the start of the irradiation and 2.51 s later. A complete study of this region has been described by Su et al. [57] in $Mg(OH)_2$ who suggest that dehydration could occur even with a very low energy current density.

From these spectra, it is possible to calculate the local relative specimen thickness before and after irradiation. In this case, the EELS measurements were taken with the electron beam parallel to [0001] direction. Applying the Kramers-Kronig sum rule [50], a relative thickness (t/λ) of ~52 nm at the beginning and ~34 nm at the end of irradiation has been obtained. The mean free path of inelastic electron scattering (MFP) calculated for 300 keV at the start of irradiation was $\lambda = 0.49$ nm and $\lambda = 0.37$ nm after 2.51 s. Thus, it has achieved a reduction around 34%, due to loss of mass during the dehydration process. Nevertheless, this reduction could not be constant and depends on several factors including the crystallographic orientation, respect to the electron beam or the acceleration voltage applied. Van Aken and Langenhorst [53] have observed a reduction about 40–50% parallel to c, in pure brucite, using 200 kV. The authors demonstrate how the relative thickness variation (t/λ) depends on the irradiation time during the dehydration process.

3.4.2. Ca L-edge

The presence of calcium has been detected in the high loss region (Ca *L*-edge, Fig. 6b) between 340 and 360 eV. At the start of irradiation (10 s), a single broad peak (347 eV) with a pre-peak (341 eV) is detected. During the dehydration process (120 s) the pre-peak increases in intensity, developing two well-defined peaks at 346 and 348 eV (the most intense).Two additional peaks of low intensity (343 and 355 eV) are formed around the most intense peak. It is noteworthy that as a result of dehydration peaks become more pronounced and narrow.

The reference pattern of the EELS database [48] also shows two distinct peaks, at 343 and 350 eV similar to the spectra after irradiation. Nevertheless, the two shoulders detected are absent in the EELS pattern. These slight differences are due to differences in

the configuration of the equipment and the incident beam energy used (200 KV).

3.4.3. O K-edge

O *K*-edge between 530 and 600 eV has been controlled along irradiation time (Fig. 6c). At the start of irradiation, three broad peaks 540 (most intense), 548 (less intense) and 559 eV (intermediate intensity) are detected. As irradiation passes, peaks tend to be more narrow and defined. This behaviour is due to the loss of water during the dehydration process. Besides, the dehydration of brucite and the resulting formation of periclase are accompanied by a rearrangement of the packing sequence of oxygen layers [52]. The reference pattern from the EELS database [48] is similar to that obtained after 120 s of irradiation and to the Van Aken and Langherhost [53] spectra after 70 s of irradiation, coinciding with the end of dehydration where the corresponding Mg–Ca oxide is formed. In the present case, the dehydration process has been slower compared to the results obtained in pure brucite [53]. Besides, although Wirth [58] has reported a pre-peak at 528 eV with 50% in height, indicating the presence of $(OH)^-$ groups or water molecules, in our study has not been detected any signal from which H behaviour could be inferred.

3.4.4. Mg K-edge

The Mg *K*-edge is located around 1320–1440 eV. The spectrum typically has three peaks. The highest intensity peak (at the left) has a pre-peak and is followed by two less intense peaks located toward the region of higher energy.

At the beginning of dehydration (10 s), the spectrum shows a main peak at 1340 eV, followed by two fairly broad peaks with low-intensity located toward the region of higher energy ($\sim$1360 and 1405 eV). This spectrum corresponds to the sample with brucite structure in its initial state before the dehydration.

At the end of dehydration (120 s), the three peaks are clearly defined, having narrow shape and increased intensity (1340, 1355 and 1410 eV respectively). The spectrum corresponds to the dehydration stage of the sample.

The comparison of the experimental spectra with the Mg *K*-edge from MgO pattern of the EELS data base [48] indicates very high similarities with the spectrum obtained at the final stage of decomposition, when the oxide is formed. Besides, this spectrum has similarities with that obtained by Van Aken and Langenhorst [53] for the dehydrated phase. However, the inversion in the order of intensities could be due to the acceleration voltage used (200 kV), the presence of structural defects and different collection conditions.

3.5. Mechanisms of dehydration

The dehydration process using an acceleration voltage of 200 kV enabled to observe gradual changes in porosity, increasing from outside to inside of the particle depending on the irradiation time. Initially, elongated pores are located at the edge of the particle. They gradually enlarge in size up to coalesce, depending on the water extraction rate from the surface, along the cleavage planes or structural defects. At the end of the irradiation, the reduction of particle volume is produced with the following formation of the Mg–Ca oxide. This is especially interesting because the porous structure in hydroxides is essential to act as catalysts and the changes in porosity could affect the catalytic performance [59]. Hence the porous architecture proves to be a key factor in controlling the chemical reactivity, the ionic exchange, the sorption processes, or the space confinement, which affect the advance rate of the transformation [60].

Similarly, $Mg_{0.97}Ca_{0.03}$ $(OH)_2$ changes its structure during dehydration. Initially, the dehydrated phase is usually placed toward the edges. Its transformation coincides with the simultaneous development of pores product of water extraction, as irradiation time increases. The penetration is not uniform and depends on various factors such as particle size, sample thickness, structural defects, crystallographic orientation, or acceleration voltage applied. Comparing the results using 200 and 300 kV, the higher the acceleration voltage, the faster is the transformation process.

The presence of water molecules in the system heavily impacts the reaction in terms of nucleation and the end product, MgO [19]. Both cationic and anionic vacancy defects are generated during the process favouring the material migration. Adsorption/desorption processes give rise to rapid crystal growth and agglomeration, with the concomitant reduction in MgO surface area [61].

Studies carried out by McKelvy et al. in pure brucite by environmental-cell (E-cell) with dynamic high resolution transmission electron microscopy [25], suggest that growth occurs via the formation of additional partial/ full oxide layers nearby, creating lamellar oxyhydroxide regions, which grow both parallel and perpendicular to the lamella in the $Mg(OH)_2$ matrix. More generally, this process exhibits primarily lamellar oxyhydroxide intergrowth or two-phase (oxide+hydroxide) behaviour via relatively slow nucleation/fast growth or fast nucleation/slow growth, respectively [25].

The kinetics for the early stages of reaction indicate a diffusion mechanism similar to the $(OH)^-$ ion migration observed in iron hydroxides [53]. The central core of hydroxide is prevented from dehydrating and the escape of water is blocked by the increasing pressure of water trapped in the outer voids which stabilizes the transformation. Then the porous microstructure is almost immediately formed and creates new surfaces in which dehydration occurs, while the retention of water within the porous structure controls the reaction rates [54]. Besides, the growth mechanism of the oxide´s rim is grain- size and surface area dependent [54], however, the presence of substitutional atoms may lead to modify the chemical centres on the surface [62]. The replacement of Mg ions by Ca ions affects the local properties of the material. Differences in the ionic radius, (Ca > Mg), could be responsible for the generation of atomic defects, which affect the kinetic of reaction modifying the hydroxide into oxide reaction time [62]. Substantial intra-lamellar strain is expected to accompany the formation of oxyhydroxide regions due to the hexagonal packing mismatch between adjacent oxide and hydroxide lamella [25].The main changes in the electronic structure are connected to differences in ion size, small modifications in the chemical bonding with local increase or decrease of the covalent character and the presence of partially filled d orbitals [62]. This small modification could affect different properties, such as the catalytic performance, which is directly related to the structure, and variation of composition in the structure [40]. In the same way that could affect it's thermal and mechanical behaviour.

Furthermore, the surfaces stability varies depending on the particles orientation, i.e. the {100} surface of rock-salt structured materials is thermodynamically more stable than {111} surface [62, 63]. In the last case, the instability of {111} orientation with an alternating array of Mg cation and O anion is due to dipole energy accumulation induced by polarity (Mg^{2+} plane and O^{2-} plane). Thus, MgO tends to grow with surface termination by {200} and their family planes to acquire the most stable atomic arrangement [64,65]. As a result, the time elapsed until the sample collapses is not the same and depends on the orientation. In the present case, less atomic defects and dislocations have been observed along the periclase basal plane, unlike octahedral surfaces, where the increase in the defects accelerates the dehydration. This transformation is faster when the octahedral surfaces are irradiated in comparison with the basal surfaces of periclase.

4. Concluding remarks

It has been successfully demonstrated that monitoring the kinetics of phase transformation and the dehydration process in Mg Ca hydroxide due to radiation damage by TEM is possible, obtaining results in short periods of time (around 2–700 s). Besides, atomic behaviour related to brucite-periclase phase transformation and advances in porosity determinations are observed using TEM-HRTEM and spectroscopy measurements (EELS-EDS).

The combining of TEM-HRTEM, EELS and image analysis techniques has been very constructive to understand the transformation mechanism from Mg–Ca hydroxide to Mg–Ca oxide produced by electron irradiation. Differences in reaction time have been observed depending on different factors; including acceleration voltage, thickness, crystalline orientation or presence of structural defects.

Specifically, It has been possible to determine reaction times during the transformation, both at 200 and 300 kV acceleration voltage, which is varying between 25, 80 and 120 s by applying 300 kV, unlike those obtained with the application of 200 kV, which last up to 700 s.

Although the $Mg_{0.97}Ca_{0.03}$ $(OH)_2$ has a similar behaviour with pure brucite($Mg(OH)_2$) during the dehydration process, the presence of calcium could not only affect the transformation time but also, cell parameters and hence its specific properties such as its catalytic behaviour. This modification depends on the calcium content in the solid solution. The control of the progressive dehydration and related changes in porosity are possible to be observed when samples are exposed to 200 kV, unlike when they are exposed to 300 kV, where the dehydration process is faster. The changes are gradual, producing an increase from the edge to the centre of the particle, depending on the irradiation time.

Different stages were observed, which are related to the amount of water extracted from the particle, until finally a decrease in porosity and particle shrinkage occurs, coinciding with the formation of the Mg–Ca oxide. HRTEM at 300 kV allows identifying different stages of transformation, determining the progressive changes from brucite to periclase, including the formation of an intermediate dehydrated brucite phase. The oxide starts to be formed at the edge of the particle, progressing inward as dehydration occurs. Based on EELS results, it has been possible to calculate a local thickness reduction of 34% in one representative particle, due to mass loss during the dehydration. Although changes in crystallinity, associated with the formation of Mg–Ca oxide, are very similar to the reported to pure brucite, the reaction times in $Mg_{0.97}Ca_{0.03}$ are slower than those reported for $Mg(OH)_2$.

Funding

This present research was funded by the Community of Madrid under the GEOMATERIALES 2 project (S2013/MIT-2914), by the Complutense University of Madrid's Research Group: "The Alteration and Conservation of Stone Heritage" (921349), the Autonomous Region Program of Madrid, MULTIMAT-CHALLENGE (ref. S2013/MIT-2862), the Innovation and Education Ministry ref. (MAT2013-47460-C5-5-P) and the Mat201019837/C06-05 projects.

Conflict of interest

The authors declare no having conflict of interest.

Acknowledgments

The authors are indebted to Laboratory Network in Science and Technology for Heritage Conservation (RedLabPat, Moncloa Campus of Excellence CEI-09-009) staff for their cooperation in this study. The assistance provided by Adrian Gómez-Herrero and Juan Luis Baldonedo of the National Microscopy Centre (Madrid, Spain) is gratefully acknowledged. Thanks go as well to A. Khalifa and P. Sierra for their assistance with the English text revision.

References

[1] F. Banhart, Electron irradiation of nanomaterials in the electron microscope, In: F. Banhart (Ed.), In-Situ Electron Microscopy at High Resolution, World Scientific Publishing Co. Pte. Ltd., London, 2008, pp. 259–295.

[2] J.D.C. McConnell, Electron-optical study of phase transformations, Min. Mag. 38 (1971) 1–20.

[3] J.W. Edington, Practical Electron Microscopy in Materials Science, Interpretation of Transmission Electron Micrographs, The Mac Millan press, London, 1975.

[4] R. Egerton, Mechanism of radiation damage in beam sensitive specimens for TEM acceleration voltage between 10 to 300 kV, Microsc. Res. Tech. 75 (2012) 1550–1556.

[5] P.A. Tamayo Meza, P. Schabes Retchkiman, L.A. Flores Herrera, V.A. Yermishkin, C.F. Ordáz Yañez, H. Sierra, Induced amorphization in pyrographite by radiation using high voltage transmission electron microscope, Adv. Mater. 284 (2011) 2026–2036.

[6] D.J. Smith, R.W. Glaisher, HREM on edge on interfaces and defects, In: D. Chems (Ed.), Evaluation of Advanced Semiconductor Materials by Electron Microscopy, Springer Science & Business Media, New York, 2012.

[7] P. Rez, J.K. Weiss, D.L. Medlin, D.G. Howitt, Direct measurements of the radiolytic transformation of thin films of titanium dioxide using EELS, Microsc. Microanal. Microstruct. 6 (4) (1995) 433–440.

[8] S.J. Chen, D.G. Howitt, B.C. Gierhart, R.L. Smith, S.D. Collins, The applications of in situ electron energy loss spectroscopy to the study of electron beam nanofabrication, Microsc. Microanal. 15 (03) (2009) 204–212.

[9] A.K. Datye, D.J. Smith, The study of heterogeneous catalysts by high-resolution transmission electron microscopy, DV, Catal. Rev. Sci. Eng. 34 (1992) 129–178.

[10] A.K. Datye, Electron microscopy of catalysts: recent achievements and future prospects, J. Catal. 216 (2003) 144–154, http://dx.doi.org/10.1016/S0021-9517(02)00113-6.

[11] G. Miehe, S. Lauterbach, H.J. Kleebe, A. Gurlo, Indium hydroxide to oxide decomposition observed in one nanocrystal during in situ transmission electron microscopy studies, J. Solid State Chem. 198 (2013) 364–370.

[12] M.S. Ball, H.F.W. Taylor, The dehydration of brucite, Mineral. Mag. 32 (1961) 754–766.

[13] M.G. Kim, U. Dahmen, A.W. Searcy, Structural transformations in the decomposition of $Mg(OH)_2$ and $MgCO_3$, J. Am. Ceram. Soc. 70 (1987) 146–154.

[14] R.W.G. Wyckoff, Crystal Structures, Robert E Krieger Publishing Company Inc, USA 1986, pp. 1897–1994.

[15] B. Mason, L.G. Bery, Elements of Mineralogy,, W.H. Freeman and Company, San Francisco, 1968.

[16] S.K. Haldar, Introduction to Mineralogy and Petrology, Elsevier, Oxford 2013, p. 354.

[17] N. Datta, S. Chatterji, J.W. Jeffery, A.L. Mackay, On the oriented transformation of Ca(OH) to CaO, Mineral. Mag. 37 (1969) 286.

[18] A.K. Galwey, M.E. Brown, Thermal Decomposition of Ionic Solids: Chemical Properties and Reactivities, Elsevier the Netherlands, Amsterdam, 1999.

[19] J. Green, Calcination of precipitated $Mg(OH)_2$ to active MgO in the production of refractory and chemical grade MgO, J. Mater. Sci. 18 (1983) 637–651.

[20] M. Müller, Symmetry relationships between crystal structures: applications of crystallographic group theory in crystal chemistry, Oxford University Press, Oxford, 2013.

[21] J.F. Goodman, The decomposition of magnesium hydroxide in an electron microscope, Proc. R. Soc. London Ser. A-Math. Phys. Sci. 247 (1958) 346–352.

[22] J.A. Wang, O. Novaro, X. Bokhimi, T. Lopez, R. Gómez, J. Navarrete, M.E. Llanos, E. López-Salinas, Structural defects and acidic and basic sites in sol–gel MgO, J. Phys. Chem. B 101 (1997) 7448–7451.

[23] A. Sierra-Fernandez, L.S. Gómez-Villalba, L. Muñoz, G. Flores, R. Fort González, M.E. Rabanal Jiménez, Effect of temperature and reaction time on the synthesis of nanocrystalline brucite, Int. J. Mod. Manuf. Technol. 6 (1) (2014) 50–54.

[24] H. Pimminger, G. Habler, N. Freiberger, R. Abart, Evolution of nanostructure and specific surface area during thermally driven dehydration of $Mg(OH)_2$, Phys. Chem. Miner. 43 (1) (2016) 59–68.

[25] M.J. McKelvy, R. Sharma, A.V. Chizmeshya, R.W. Carpenter, K. Streib, Magnesium hydroxide dehydroxylation: in situ nanoscale observations of lamellar nucleation and growth, Chem. Mater. 13 (3) (2001) 921–926.

[26] S.B. Vendelbo, P.J. Kooyman, J.F. Creemer, B. Morana, L. Mele, P. Dona, B. J. Nelissen, S. Helveg, Method for local temperature measurement in a nanoreactor for *in* situ high resolution electron microscopy, Ultramicroscopy 133 (2013) 72–79.

[27] M.A. Asoro, P.J. Ferreira, D. Kovar, In situ transmission electron microscopy and scanning transmission electron microscopy studies of sintering of Ag and Pt nanoparticles, Acta Mater. 81 (2014) 173–183.
[28] N. Thangaraj, K.H. Westmacott, U. Dahmen, HVEM studies of the sintering of MgO nanocrystals prepared by $Mg(OH)_2$ decomposition, Ultramicroscopy 37 (1) (1991) 362–374.
[29] P. Baglioni, R. Giorgi, Soft and hard nanomaterials for restoration and conservation of cultural heritage, Soft Matter 2 (4) (2006) 293–303.
[30] G.J. Simandl, S. Paradis, M. Irvine, Brucite-industrial mineral with a future, Geosci. Can. 34 (2007) 57–64.
[31] Y. Zhang, M. Ma, X. Zhang, B. Wang, R. Liu, Synthesis, characterization, and catalytic property of nanosized MgO flakes with different shapes, J. Alloy. Compd. 590 (2014) 373–379.
[32] Ch Schacht, Refractories Handbook, Marcel Dekker Inc. CRC Press, USA, 2004, ISBN 08247.5654-1.
[33] Y. Zhang, T. He, W. Cao, Y. Cheng, X. Zhang, Study on application of brucite fiber to composite paint with energy-saving and thermal insulation, New Build. Mater. 8 (2007) 026.
[34] J. Formosa, J.M. Chimenos, A.M. Lacasta, L. Haurie, Thermal study of low-grade magnesium hydroxide used as fire retardant and in passive fire protection, Thermochim. Acta. 515 (2011) 43–500.
[35] M.A. Shand, The Chemistry and Technology of Magnesia, John Wiley & Sons, Inc, New Jersey, 2006.
[36] B.S. Necula, L.E. Fratila-Apachitei, A. Berkani, I. Apachitei, J. Duszczyk, Enrichment of anodic MgO layers with Ag nanoparticles for biomedical applications, J. Mater. Sci. -Mater. Med. 20 (2009) 339–345.
[37] K. He, Y.M. Dong, Z. Li, L. Yin, A.M. Zhang, Y.C. Zheng, Catalytic ozonation of phenol in water with natural brucite and magnesia, J. Hazard. Mater. 159 (2) (2008) 587–592.
[38] H.U. Rammelberg, J.K. Köllner, T. Schmidt, O. Opel, W. Ruck, Hydration and dehydration of salt hydrates and hydroxides for thermal energy storage kinetics, energy release and cyclability, Appl. Energy (2015), http://dx.doi.org/10.1016/j.apenergy.2015.02.011.
[39] M. Zamengo, J. Ryu, Y. Kato, Chemical heat storage of thermal energy from a nuclear reactor by using a magnesium hydroxide/expanded graphite composite material, Energy Procedia 71 (2015) 293–305.
[40] L.D. Francis, J. Rivas, M.J. Yacamán Understanding the structure of nanocatalysts with high resolution scanning/transmission electron microscopy, IOP Conf. Series: Materials Science and Engineering 55 (2014). doi:10.1088/1757-899X/55/1/012005.
[41] Y. Castro, A. Durán, Mesoporous and mesostructured TiO_2 coatings for photocatalytic applications, J. Sol–Gel Sci. Technol. 70 (2) (2014) 254–262.
[42] F. Cardarelli, Materials Handbook: A Concise Desktop Reference, Springer, London, 2008, 1339p.
[43] R.H. Vernon, Metamorphic Processes, George Allen and Unwin, London, 1976.
[44] A. Sierra-Fernandez, L.S. Gomez-Villalba, M.E. Rabanal, R. Fort, New consolidant product based on nanoparticles to preserve the dolomitic stone heritage, In: M. Rogerio Candelera (Ed.), Science, Technology and Cultural Heritage, 2014, pp. 139–144, ISBN 9781315712420.
[45] L. Dei, Conservation treatments: cleaning, consolidation and protection, In: Nanoscience for the Conservation of works of Art, In: P. Baglioni, D. Chelazzi (Eds.), Nanoscience & Nanotechnology 28, The Royal Society of Chemistry, Cambridge, 2013, pp. 77–92.
[46] A. Sierra-Fernandez, L. Csóka, L.S. Gomez-Villalba, R. Fort, M.E. Rabanal, Innovative Inorganic Nanomaterial for the conservation of Cultural Heritage, In: Proceedings of the 14th International Conference of the European Ceramic Society, Toledo, Spain, 2015.
[47] R. Giorgi, C. Bozzi, L.G. Dei, C. Gabbiani, B.W. Ninham, P. Baglioni, Nanoparticles of $Mg(OH)_2$: synthesis and application to paper conservation, Langmuir 21 (2005) 8495–8501.
[48] EELS database, EMES and IMN laboratories, the European microscopy network ESTEEM 2, the French microscopy network METSA and by the French microscopy society SFμ ⟨⟨https://eelsdb.eu/⟩⟩.
[49] J.P. Morniroli, D. Vankieken, Microdiffraction as a tool for crystal structure identification and determination, Ultramicroscopy 45 (2) (1992) 219–239.
[50] R. Egerton, Electron energy-loss spectroscopy in the TEM, Rep. Prog. Phys. 72 (2009) 25.
[51] A.J. Garvie, Can electron energy-loss spectroscopy (EELS) be used to quantify hydrogen in minerals from the O K edge? Am. Miner. 95 (2010) 92–97.
[52] R.T. Shannon, Revised effective ionic radii and systematic studies of interatomic distances in halides and chalcogenides, Acta Crystallogr. Sect. A: Cryst. Phys., Diffr., Theor. General. Crystallogr. 32 (5) (1976) 751–767.
[53] P.A. Van Aken, F. Langenhorst, Nanocrystalline, porous periclase aggregates as product of brucite dehydration, Eur. J. Miner. 13 (2001) 329–341.
[54] C.J. Goss, The kinetics and reaction mechanism of the goethite to hematite transformation, Miner. Mag. 51 (1987) 437–451.
[55] M.P. Rosynek, D.T. Magnuson, Preparation and characterization of catalytic lanthanum oxide, J. Catal. 46 (3) (1977) 402–413.
[56] J.D. Bernal, D.R. Dasgupta, L. Mackay, The oxides and hydroxides of iron and their structural inter-relationships, Clay Min. Bull. 4 (21) (1958) 15–30.
[57] D. Su, N. Jiang, J.C.H. Spence, F. He, W.T. Petuskey, On the dehydration of $Mg(OH)_2$ by a high-energy electron beam, J. Appl. Phys. 104 (2008) 063514.
[58] R. Wirth, Water in minerals detectable by electron energy-loss spectroscopy EELS, Phys. Chem. Miner. 24 (1997) 561–568.
[59] R. Lianga, G. Wang, X.L. Huang, Li Zhu, Y. Yan, B. Zhong, Improving the specific capacitance of $Ni(OH)_2$-based supercapacitors by tailoring its porous structures and particle size, Mater. Lett. 158 (1) (2015) 128–131.
[60] H.C. Zeng. Nanostructured Catalytic Materials: Design and Synthesis, In: Dekker Encyclopedia of Nanoscience and Nanotechnology, Second ed. 2004, pp. 2539-2550. ISBN: 0-8493-9639-5, eISBN: 0-8493-9638-7 DOI: 10.1081/E-ENN2-120009427.
[61] P.J. Anderson, P.L. Morgan, Effects of water vapour on sintering of MgO, Trans. Faraday Soc. 60 (1964) 930–937.
[62] G. Pacchioni, Theory of metal clusters on the MgO surface: the role of point defects, In: U. Heinz, U. Landman (Eds.), Nanocatalysis, Springer, Berlin Heidelberg New York, 2007, pp. 208–209.
[63] R.A. Wogeliljs, K. Refson, D. Fraser, G.W. Grime, J.P. Goff, Periclase surface hydroxylation during dissolution, Geochim. Cosmochim. Acta 59 (1995) 1875–1881.
[64] Son Jun Ho, Yu. Hak Ki, Lee Jong-Lam, MgO nano-pyramids structure for enhancement of light extraction efficiency in vertical light emitting diodes, Opt. express A 18 (103) (2010) 403–410.
[65] X.-S. Fang, C.-H. Ye, L.-D. Zhang, J.-X. Zhang, J.-W. Zhao, P. Yan, Direct observation of the growth process of MgO nanoflowers by a simple chemical route, Small 1 (4) (2005) 422–428.